



PAPER • OPEN ACCESS

3D melt electrowritten MXene-reinforced scaffolds for tissue engineering applications

To cite this article: Mahdiyeh Zahrabi et al 2025 Biofabrication 17 045011

View the article online for updates and enhancements.

You may also like

- Thermally stable, photocrossinkable and biocompatible copolymers for melt electrowriting
 Sean O Mathew Ronghui Oi and Brian G
- Sean O Mathew, Ronghui Qi and Brian G Amsden
- Melt electrowriting of poly(caprolactone)—poly(ethylene glycol) backbone polymer blend scaffolds with improved hydrophilicity and functionality Conor Darroch, Francesco Digeronimo, Giuseppe Asaro et al.
- Fabrication of human myocardium using multidimensional modelling of engineered tissues

Pilar Montero-Calle, María Flandes-Iparraguirre, Konstantinos Mountris et al.

Biofabrication



OPEN ACCESS

RECEIVED

26 February 2025

REVISED

18 June 2025

ACCEPTED FOR PUBLICATION

5 August 2025

PUBLISHED

22 August 2025

Original content from this work may be used under the terms of the Creative Commons Attribution 4.0 licence.

Any further distribution of this work must maintain attribution to the author(s) and the title of the work, journal citation and DOI.



PAPER

3D melt electrowritten MXene-reinforced scaffolds for tissue engineering applications

Mahdiyeh Zahrabi^{1,2}, Mine Altunbek¹, Süleyman Çelik¹, Mina Namvari^{1,*} and Bahattin Koc^{1,2,3,*}

- ¹ Sabanci University Nanotechnology Research and Application Center, Istanbul 34956, Turkey
- ² Sabanci University Faculty of Engineering and Natural Sciences, Istanbul 34956, Turkey
- Sabanci University Integrated Manufacturing Technologies Research and Application Center, Istanbul 34906, Turkey
- * Authors to whom any correspondence should be addressed.

E-mail: bahattinkoc@sabanciuniv.edu and mina.namvari@sabanciuniv.edu

Keywords: MXene, melt electrowriting, PCL Scaffold, tissue engineering

Supplementary material for this article is available online

Abstract

 $2D Ti_3C_2T_x$ (MXene) is attracting significant attention in tissue engineering. The incorporation of these promising materials into conventional scaffolds remains challenging, particularly with physicochemical properties compatible with biological systems. Melt electrowriting (MEW) has emerged as a powerful additive manufacturing technique for biofabrication of customized three-dimensional (3D) scaffolds composed of bioactive materials. This study introduces MEW of 2D MXene and polycaprolactone (PCL) nanocomposite scaffolds for tissue engineering applications. First, $Ti_3C_2T_x$ was functionalized using (3-aminopropyl) triethoxysilane (referred to as f-MXene) to obtain a blended nanocomposite in PCL matrix (referred to as MX/PCL). Fourier transform infrared spectroscopy revealed the nanocomposite composition. X-ray diffraction analysis showed the reduced crystallinity in PCL after incorporation of f-MXene. Differential scanning calorimetry helped to establish the optimal MEW parameters. Thermogravimetric analysis conducted on nanocomposites containing 0.1, 0.5, and 1% (w/w) f-MXene showed the thermal stability of MXene during the MEW process. The extrudability and printability of the nanocomposites with varying concentrations was demonstrated using MEW in 0-90-degree mesh scaffolds with fine filament dimensions. Scanning electron microscopy and Energy-dispersive x-ray spectroscopy mapping showed the shape fidelity, printing accuracy, and structural integrity of 3D MEW scaffolds with uniform distribution of f-MXene, respectively. Further characterization showed the concentration-dependent enhancement in hydrophilicity and compressive modulus and yield strength of scaffolds upon integration of f-MXene. Atomic force microscopy analysis demonstrated that the topography of the 3D MEW MX/PCL scaffolds changed compared to the pristine PCL and the roughness of the surfaces increased as the concentration of the f-MXene increased. Accelerated degradation tests demonstrated that increasing filler concentration in the reinforced scaffolds progressively delayed degradation compared to the control. The in vitro characterization showed the adherence of MC3T3-E1 preosteoblast cells on MX/PCL scaffolds and their enhanced osteogenic differentiation. The findings indicate that 3D printed MX/PCL nanocomposite scaffolds have significant potential as mechanically robust scaffolds with controlled degradation rate and cytocompatibility for tissue regeneration, with properties tunable for specific applications.

1. Introduction

Tissue engineering presents remarkable advancements in regenerative medicine by offering novel solutions for repairing or replacing diseased tissues and organs. The primary goal is to fabricate scaffolds that can provide a biomimetic extracellular matrix (ECM) environment optimal for cell adhesion, proliferation, migration, and differentiation [1-7]. Three-dimensional (3D) printing technology offers the advantage of fabricating tissue scaffolds with welldefined dimensions, greater precision, and intricacy, and compatibility with human tissues in both biological and mechanical properties [8-11]. Extrusionbased 3D printing, namely fused deposition modeling (FDM), is the most used approach that involves the extrusion of ink through a mobile nozzle guided by the computer aided-3D design to construct a structure by layer-by-layer deposition. Nevertheless, this approach faces difficulties when it comes to printing small filaments, especially when fabricating nanocomposites with higher viscosity compared to pristine polymers [12, 13]. Melt electrowriting (MEW) is a highly promising technique for fabricating 3D structures composed of microscale fibers. The process combines FDM with solution electrospinning. In this technique, the melted polymer is extruded through the nozzle with accurate control of fiber deposition, geometry, and pore size under high voltage to construct the scaffolds with micro-sized fibers [14, 15].

Polycaprolactone (PCL) is a widely used synthetic thermoplastic polymer in biomedical applications that has received approval from the Food and Drug Administration. It has been most frequently utilized in the manufacturing of tissue scaffolds and 3D MEW printing due to its low melting point of 60 °C [8, 16-18]. Since PCL is an implantable synthetic polymer, its degradation mechanism and breakdown process have been thoroughly investigated [19]. Furthermore, PCL is a stiff polymer that can form sharp edges as it breaks down due to a rapid decrease in molecular weight (MW). This might lead to unwanted inflammation in the surrounding tissues [19, 20]. Therefore, 3D PCL scaffolds with optimal size, shape, and biocompatibility are essential for effective tissue regeneration. Addressing all processing for biological and mechanical properties of PCL scaffolds remains a challenge, driving ongoing research into optimal material compositions and processing conditions. Typical strategies include printing PCL using MEW to achieve smaller filament diameters, which can potentially modify the degradation profile, while incorporating bioactive materials into the polymer matrix for substantial improvements in surface roughness, hydrophilicity, and protein adsorption are crucial for facilitating cell attachment and proliferation [21]. Combining polymeric materials with other 2D materials such as graphene nanosheets [22], graphene oxide [23], graphene nanoplatelets [24], and graphene quantum dots [25] has shown to improve its mechanical, thermal, and biological properties.

MXene has gained significant received notable interest in as fillers for polymer matrices [26]. As a novel 2D structures with exceptional electrical, thermal, and mechanical characteristics, it have received notable interest and have been thoroughly examined in the realm of tissue engineering [27]. MXenes are materials with the formula $M_{n+1}X_nT_x$, where M represents an early transition metal (Ti, Zr, Cr, V, Hf, Nb, Sc, Ta, Mo), X is carbon and/or nitrogen, and T_x denotes surface terminations. Commonly synthesized through a top-down process involving selective etching of the Al from the commercially available precursor MAX phases (Ti₃AlC₂) using fluoride-containing reagents, MXenes exhibit terminated surfaces with functional groups like -OH, -Cl, and -F [28]. Since the first attempt [29], MXene has consistently been compared to graphene due to its shared characteristics. Both are 2D ultrathin nanoflakes, as evidenced by the suffix 'ene' in their names. Nevertheless, MXene surpasses graphene in certain aspects. For instance, MXene exhibits superior biocompatibility at higher concentrations [30]. Among the 2D materials beyond graphene, MXenes have been investigated in various fields over the past decade since their discovery. These materials have been studied in energy storage [31, 32], optoelectronics [33], electromagnetic interference shielding [7], wearable sensors [34], tissue engineering [35], thermal management [36], and water remediation [37] due to their metallike conductivity, hydrophilicity, solution processability, enhanced mechanical properties, photoand electrothermal characteristics, and antibacterial properties.

Integrating MXene into polymer matrices has demonstrated enhanced cell adhesion and proliferation while maintaining cell viability [38]. Specifically, the existence of surface imperfections and functionalities can influence the wetting properties of surfaces, which subsequently impact their biocompatibility [39]. In particular, Ti-based species released when water and oxygen interact with MXene can promote cell growth [40]. Additionally, Ti₃C₂T_x was reported to enhance osteogenic differentiation of hPDLCs, thereby facilitating the regeneration of periodontal tissue [41]. Another study found that MXene altered the metabolic activities in neural stem cells by decreasing glucose and increasing lactic acid when electric stimulation was applied [42]. Moreover,

MXenes exhibit versatile functional groups for tailored biological interactions and can be modified with bioactive molecules for further functionalities in tissue engineering. MXenes offer good strength and better flexibility in composites and possess inherent antibacterial properties, as well as excellent antioxidation and anti-inflammatory properties useful for cellular activities [43]. Research has shown that MAXphases [44, 45] and MXenes [46, 47] significantly contribute to bone formation via bio-absorption and bioactivity [47]. This indicates the necessity of regulating the quantity of MAX-phases and MXenes as composite reinforcement, which is crucial for influencing the resultant mechanical and biological performance. Diedkova et al [39] investigated the synthesis of PCL-MXene nanofibrous scaffolds via dipcoating electrospun PCL membranes into MXene dispersion, demonstrating that MXene sheets densely cover the surface of the PCL nanofibers. The study highlighted the potential of these scaffolds to support cell adhesion and proliferation, which are essential for effective tissue regeneration. Similarly, Nan et al [48] spray-coated MXene onto electrospun PCL underscoring the potential of the composite to enhance neurite regeneration and angiogenesis. Li et al [49] coated the melt-electrowritten PCL scaffold with MXene for guided neuronal growth. While these studies showcased various strategies to incorporate MXene into scaffolds, challenges remain in achieving robust, bioactive scaffolds via 3D printing of MXene/PCL composites, particularly in controlling MXene loading and ensuring its homogeneous dispersion within the hydrophobic PCL matrix.

The integration of hydrophilic MXenes into hydrophobic PCL matrices is hindered by poor dispersion. The amine functional group of (3aminopropyl) triethoxysilane (APTES) can improve the surface hydrophobicity of MXene [50-52]. This approach promises better dispersion of MXene in PCL and enables the fabrication of MXene/PCL nanocomposite scaffolds using MEW. However, to the best of our knowledge, there are no reports on MXene/PCL composites manufactured using 3D MEW in the literature. This study represents the first demonstration of MXene-reinforced PCL nanocomposite scaffolds fabricated using MEW, introducing a novel nanocomposite scaffold with biocompatible and osteoinductive properties. The 0-90° mesh architecture was selected to create a homogeneous porous structure that facilitates tissue infiltration [1-3]. First, MXene was functionalized with APTES as a favored silane coupling agent (f-MXene). This modification enhanced the integration of MXene into the PCL matrix. The obtained composites (MX/PCL) were thoroughly characterized using FTIR analysis, SEM, XRD, TGA, and EDS.

Scaffolds with \sim 100 μ m fiber diameter and final pore size of \sim 700 μ m was printed to evaluate the specific influence of MXene incorporation on MEW MX/PCL scaffolds. The later architectural optimization could introduce additional architectural variables that might obscure the direct assessment of MXene's bioactivity for different tissue engineering applications.

MX/PCL nanocomposite scaffolds were 3D printed by arranging approximately 100 μ m fibers in a 0–90-degree mesh structure with final pore size of 700 μ m using MEW. The inter-filament spacing in our design was selected to create a homogeneous porous structure and to evaluate precise filament deposition of MX/PCL nanocomposites. However, this technique offers flexibility for creating different designs suitable for balanced structural integrity and cell migration. The design can be further optimized based on various application requirements.

Subsequently, 3D-printed MEW nanocomposite scaffolds were characterized for their mechanical behavior, hydrophilicity, and accelerated degradation rate. *In vitro* analyses included cell adhesion, morphology, alkaline phosphatase (ALP) activity and mineralization. The findings showed that the unique microstructure and composition of the MX/PCL scaffolds are promising candidates for bone tissue engineering applications.

2. Materials and methods

2.1. Materials

PCL Capa 6400 (MW of 37 000 g mol⁻¹) was obtained from Capa Perstorp Ltd, UK. Ti₃AlC₂ (MAX phase) (325 Mesh, Purity: 99+%) was purchased from Nanografi (Ankara, Turkey). Lithium fluoride (LiF, 300 mesh) and concentrated HCl were obtained from ThermoFisher Scientific and Merck, respectively. APTES (99%), Trypsin-EDTA solution, Penicillin Streptomycin, paraformaldehyde (PFA), and Alizarin Red S, were purchased from Sigma Aldrich. MC3T3-E1 Subclone 4 preosteoblast cells were obtained from ATCC. Alpha-MEM Medium, M-PER™ Mammalian protein extraction reagent, and Bicinchoninic acid (BCA) protein test kit Bovine serum albumin (BSA) was purchased from Thermofisher Scientific. Fetal bovine serum (FBS) was provided by Pan Biotech. Triton X-100 was obtained from AppliChem. Calcein-AM (green fluorescence) was purchased from Life technologies. Propidium iodide was obtained from Invitrogen. Alexa Fluor® 546 Phalloidin and 4',6-diamidino-2-phenylindole (DAPI) were purchased from Life Technologies and Thermo fisher, respectively. pnitrophenyl phosphate (pNPP) liquid substrate system was provided by Sigma. PBS tablets were obtained from MP Biomedicals, LLC.

2.2. Synthesis of MXene

MXene was synthesized according to a previous literature report [53]. A total of 2 g of LiF was mixed with 40 ml of 6 M HCl and stirred for 10 min. Subsequently, 2 g of Ti₃AlC₂ powder was gradually introduced into the mixture and agitated at a temperature of 40 °C for 45 h. Following the etching procedure, the sediments obtained were rinsed several times using deionized water and subjected to centrifugation at a speed of 3500 rpm for a duration of 5 min, until the pH approached nearly 6. Additional water was introduced to the sediment, which was then bath sonicated for 30 min under N₂ gas and centrifuged at a speed of 10 000 rpm for a duration of 30 min to collect the supernatant as MXene. The final product was obtained by freeze-drying over a period of 3 d.

2.3. Synthesis of APTES-functionalized MXene (*f*-MXene)

100 mg MXene was dispersed in absolute ethanol and deionized water (9:1 v/v%, 50 ml) under N_2 gas for 30 min using bath sonication. The dispersion was kept at pH 3-4 by adding glacial acetic acid. Next, APTES was introduced to the dispersion at a 2:1 ratio (w/w). The resulting suspension was stirred at room temperature for 24 h. Then, it was rinsed with ethanol and water (three times each) before freeze-drying to obtain f-MXene [52].

2.4. Preparation of MX/PCL composites

PCL is a thermoplastic polymer widely used in the biofabrication of scaffolds due to its mechanical properties, which are well-suited for bone tissue engineering applications. However, PCL exhibits a long degradation profile (approximately 2–3 years) that cannot be effectively simulated under laboratory conditions using physiological solutions such as PBS or simulated body fluids. As an alternative, high-concentration NaOH solutions are often employed to accelerate the hydrolytic degradation of PCL-based tissue scaffolds [54].

Various PCL and *f*-MXene concentrations were prepared in acetone to achieve a final 10 %, (w/v) nanocomposite as described in table 1. Briefly, 0.1, 0.5, and 1% (w/w) *f*-MXene were thoroughly dispersed into acetone and probe sonicated for 15 min, separately. To increase the compatibility, PCL pellets were treated with 2 M NaOH for 2 h before mixing with *f*-MXene in acetone. The corresponding amount of NaOH-treated PCL as given in table 1 was added to each dispersion and stirred until the solution became homogeneous. Pristine PCL solution in acetone was prepared as control. Obtained pristine and nanocomposite polymer solutions were poured into glass containers and allowed to dry and ensure complete evaporation of acetone under vacuum for 2 h (figure 1).

Table 1. The concentration of PCL and f-MXene in nanocomposite.

Material	PCL (w/w %)	f-Mxene (w/w %)	
Pristine PCL	100	0.00	
0.1% MX/PCL	99.90	0.10	
0.5% MX/PCL	99.50	0.50	
1% MX/PCL	99.00	1.00	

2.5. MEW of nanocomposites

2.5.1. Design of experiment for comparing printability of MX/PCL nanocomposites

To better understand how printing parameters influence the fiber diameter of various MXene/PCL nanocomposites, we conducted a design of experiment. This analysis included key parameters such as printing speed, nozzle-to-collector distance, feeding pressure, and acceleration voltage, each tested over a defined minimum and maximum range. The RSM framework allowed us to establish a baseline set of experiments to obtain a model describing how fiber diameter varies across different concentrations of MXene and printing parameter settings, accounting for the distinct behaviors of nanocomposites introduced by MXene's incorporation. Sets of experimental runs were designed, with varying printing parameters—collector speed, nozzle-to-collector distance, feeding pressure, and acceleration voltage. These parameters were held constant for all concentrations to isolate material effects.

2.5.2. Optimized printing parameters

We developed a path planning tool to fabricate 0-90-degree mesh 3D structures with interconnected porosity, uniform arrangement and structural uniformity. Scaffolds measuring $35 \times 35 \text{ mm}^2$ were produced using the specified parameters in table 2, consisting of 6 layers. The morphology of the 3D-printed scaffolds was analyzed using FE-SEM analysis. To fabricate the scaffolds, PCL and MX/PCL nanocomposites were placed in stainless steel syringe barrels, preheated at 70 °C-75 °C for 2 h, and extruded through a 250 μ m nozzle. Various pressures were originally tested to identify the corresponding optimal conditions for high-resolution printing of all groups with desired diameter, maintaining a constant feed rate of 110 mm min $^{-1}$, an applied voltage of 4–5 kV, and a nozzle-to-substrate gap of 2.5-3 mm. After determining the optimum pressure required for smooth filament extrusion, this pressure was fixed across each material composition to produce straight, continuous filaments at each concentration.

To enable the full formation of a crystalline structure, the polymer melt in the syringe reservoir was cooled gradually below the crystallization temperature between each run. Thermal history and processing circumstances have a major impact on the



Figure 1. Schematic illustration of MX/PCL nanocomposites preparation. (1) MXene was functionalized using APTES (2) f-MXene was dispersed in acetone and subjected to probe sonication, and PCL was separately dissolved in acetone and mixed with the f-MXene dispersion to achieve final concentrations of 0.1, 0.5, and 1.0% (w/w). (3) The vacuum dried nanocomposite was used to construct scaffolds via 3D MEW.

Table 2. Printing parameters of MX/PCL nanocomposites with various concentrations.

Scaffold	Printing speed (mm min ⁻¹)	Printing temperature (°C)	Feeding pressure (bar)	Nozzle And collector distance (mm)	Acceleration voltage (KV)
Pristine PCL	110	70	1.5	3	4-5
0.1% MX/PCL	110	70	1.6	2.8	4-5
0.5% MX/PCL	110	75	1.8	2.6	4-5
1% MX/PCL	110	75	2	2.5	4-5

repeatability of the 3D printing process and the uniformity of the flow characteristics. The syringe reservoir ensured a full crystalline structure prior to each printing trial and reduced the amount of change in the flow profile.

2.6. Characterizations of synthesized MXene, f-MXene, and MX/PCL composites

2.6.1. XRD and FTIR analyses

MAX phase, MXene, and f-MXene were characterized by XRD (Bruker D2 Advance, Germany) with a monochromatized Cu-K α radiation ($\lambda = 1.54184$ Å) generated at 30 kV and 10 mA, at a scan rate of 1° min⁻¹ and a step size of 0.02.

The chemical compositions were analyzed using attenuated total reflectance/Fourier transform infrared spectroscopy (ATR/FTIR) with a NicoletTM iS10 instrument from Thermo ScientificTM in the USA. Within the spectral region of 800–2000 cm $^{-1}$, a total of 128 scans were conducted.

2.6.2. TGA and Differential scanning calorimetry (DSC) analyses

The thermal gravimetric analysis was conducted under an air environment, with a flow rate of 60 ml min⁻¹, and a temperature range of 25–700 °C in an inert atmosphere using Q500 TGA (TA Instrument, USA). The temperature increased at a rate of 10 °C min⁻¹.

DSC analysis was performed by using a DSC 204 F1 Phoenix (NETZSCH, Weimar, Germany) in two cycles at 10 °C min⁻¹ under a nitrogen atmosphere. The sample pre-sealed in an aluminum pan was first heated to 80 °C (above the melting point of the polymer) and then cooled to -30 °C to record melting and crystallization peaks.

2.7. Characterizations of 3D-printed MEW scaffolds

2.7.1. SEM and EDS analysis

The morphological characterization of the 3D MEW pristine and nanocomposite scaffolds was conducted using SEM images (FESEM, Zeiss Leo Supra VP). The fiber diameter and spacing were quantified from the SEM images using ImageJ software. SEM/EDS analysis was performed to determine the material composition in extruded filaments. Prior to SEM/EDS analysis, the scaffolds were mounted on conductive carbon tape strips. The tilted top views of scaffolds were obtained. All samples were coated with gold particles using a Cressington 108 sputter coater to improve their conductivity and, consequently, the imaging quality.

2.7.2. AFM analysis

High Perfomance AFM (NanoMagnetics Instruments) was used to analyze the surface topography on the fiber surface of MEW scaffolds. A 5 \times 5 μ m area from different regions was scanned with 20 μ m s⁻¹ in dynamic mode using a gold-coated

silicon cantilever. Three replicates *were* used to calculate average surface roughness. The data represented as the mean \pm standard deviation).

2.7.3. Mechanical test

The mechanical properties of 3D-printed pristine and MX/PCL scaffolds with various compositions were evaluated through a uniaxial compression test utilizing a dynamic mechanical analyzer (DMA, Mark10) a 1 kN load cell in dry state. Circular samples (n = 5) were prepared with thickness of 2 mm, and diameter of 5 mm. The specimen were cut from larger scaffolds using puncher with inner diameter of 5 mm. Scaffolds were subjected to compression at a strain rate of 0.01 mm s⁻¹ until 80% deformation. Finally, compressive modulus was calculated from the slope of the strain–stress curve in the linear region and yield strength was calculated as the maximum amount of load material can take before it begins to yield and permanently deform.

2.7.4. Contact angle measurement and hydrophilicity The hydrophilicity of the nanocomposites was evaluated using water contact angle (WCA) measurement (Terra Lab, Turkey). A 4 μ l droplet of deionized water was deposited on the surface of the 3D-printed MEW Pristine PCL and MX/PCL scaffolds. The contact angle measurements were reported as the mean \pm standard deviation.

2.7.5. Accelerated degradation

Scaffolds for each condition were submerged in a solution of 5 M sodium hydroxide (NaOH), kept at a temperature of 37 °C, and taken out at specific time intervals of 24, 36, 48, 72, and 96 h, before being freeze-dried to observe the accelerated deterioration process. We employed the following equation to compute the percentage of degradation.

$$D(\%) = \left(\frac{W_d}{W_0}\right) * 100.$$

The equation uses the variable W_0 to represent the initial weight of the sample before deterioration, and W_d to represent the weight that remains after degradation. The degradation experiments were carried out with four repetitions for each condition, and the mean data was utilized to create the degradation plots.

2.8. In-vitro studies

2.8.1. Cell culture

MC3T3-E1 preosteoblast cells were maintained in Alpha-MEM medium supplemented with 10% FBS and 1% penicillin-streptomycin. The cells were expanded in a humidified and CO₂ supplemented 37 °C incubator and split into larger flasks when they reached 80%–90% confluency. Prior to cell seeding, the MEW scaffolds were sterilized by immersing them in 70% ethanol for 15 min and exposing them to

UV radiation for 30 min on each side. Subsequently, the scaffolds were placed on a PDMS-coated plate and approximately 1 million MC3T3-E1 preosteo-blast cells were seeded on the scaffolds for two hours [55]. Afterward, they were transferred to a non-cell-adhesive 96-well plate and incubated in a humidified environment at 37 °C with 5% CO2 for further analysis. The medium was changed every other day.

2.8.2. F-actin/Nuclei staining

Phalloidin/DAPI staining was performed to examine cell adhesion and morphology on the surface of the pristine and nanocomposite scaffolds by day 21. The samples were treated with 4% PFA for 30 min on day 7, 14, and 21. The cell membranes were permeabilized by treating them with a solution containing 0.1% Triton-X 100 in PBS for 10 min, followed by rinsing. The samples were treated with a red, fluorescent dye called Alexa-Fluor 568 phalloidin conjugate (Abcam, UK) to stain the F-actin. After 45 min of incubation at room temperature, the samples were rinsed with PBS. The cell nuclei were stained with 4',6-diamidino-2phenylindole (DAPI) for 15 min and subsequently rinsed with PBS. All the operations were conducted at ambient temperature and according to the manufacturer's protocol. Afterward, a Carl Zeiss LSM 710 laser confocal microscope was used to collect z-stacks images of the scaffolds.

2.8.3. ALP enzymatic activity for osteogenic differentiation

ALP activity was assessed on days 7, 14, and 21 of incubation. First, the samples were exposed to M-PER™ Mammalian Protein extraction reagent for 30 min at room temperature to lyse the cells. Then, the lysis solutions were subjected to centrifugation at a speed of 14 000 rpm for 15 min. The resulting supernatant was then placed in a solution containing pNPP and incubated at a temperature of 37 °C. After the 60 min incubation, the absorbance of the solution was measured at a wavelength of 405 nm. The protein content of each sample was quantified using the BCA Protein assay kit. In summary, BSA solutions with a concentration range of 5-1000 g ml⁻¹ were utilized to produce protein standards. the The data obtained from BCA test were utilized to standardize the ALP activity based on the protein content per mg.

2.8.4. Alizarin red staining

The composite scaffolds were subjected to staining using prepared Alizarin Red to verify the presence of calcium (Ca) mineralization. The structures were initially stained with Alizarin Red S solution (2 mg ml⁻¹, pH: 4.1–4.2) for 1 min. After washing with distilled water, digital images of all scaffolds were captured using a long working distance digital microscope (Dino-lite AM4113TR4).

2.9. Statistical analysis

The statistical significance of the results was calculated using GraphPad Prism 6.0. One-way ANOVA and two-way ANOVA analyses with Tukey tests were performed. Data were represented as mean \pm standard deviation and *p < 0.05, **p < 0.01, ***p < 0.001, and ****p < 0.0001 were considered statistically significant changes.

3. Results and discussion

3.1. Characterizations of synthesized MXene and f-MXene

MXene was synthesized by etching Al from the MAX phase (Ti₃AlC₂) with a series of controlled treatments with LiF/HCl by following the well-optimized procedure in the literature [53]. The synthesized Ti₃C₂Tx MXene was then modified with APTES (f-MXene) to achieve a compatible chemical property for further printing applications within PCL matrix. Figure 2 displays SEM images, XRD analysis and FTIR spectra acquired for the MXene and f-MXene. SEM images showed that the obtained MXene was in an intact 2D structure with Ti, O, C, and F elemental composition (figure 2(A), i-ii-iii-iv, respectively). The MXene was successfully modified with APTES, but the intact structure crumbled and became rougher [56] revealed by the SEM in figure 2(B). EDS mapping demonstrated the successful modification with positive signals from Si and N elements (figure 2).

XRD analysis provided comprehensive insights into the structural characteristics of synthesized materials, including MAX phase, MXene, and f-MXene in figure 2(C). The diffraction pattern of the MAX phase displays sharp peaks at 20 values around 9.5° (002), 19.1° (004), and 38.7° (104), indicative of a well-defined crystalline structure of the MAX phase precursor. After the etching process and the removal of the Al layer, the absence of (104) peak and the shift and broadening in (002) peak indicate the synthesis of MXene [52]. The surface modification of MXene with APTES results in a further shift in (002) peak to lower angles, approximately $2\theta = 5.6^{\circ}$, signifying an increase in interlayer spacing (d-spacing) due to functionalization [52]. The d-spacing of MAX-phase, MXene and f-MXene are calculated using the Bragg equation as 9.1 Å for MAX phase, 12.52 Å for MXene, and 15.22 Å for APTES-MXene [28].

FTIR spectra acquired for the MXene and *f*-MXene are displayed in figure 2(d). The peaks seen in the spectrum of MXene nanosheets at 1650 cm⁻¹ and around 3400 cm⁻¹ correspond to the hydroxyl group and contribute to the increased the hydrophilicity of the produced MXene. The peaks corresponding to the hydroxyl group in the spectrum of MXene nanosheets exhibit a high intensity, indicating the effective production of MXene. The 597 cm⁻¹ peak observed in

the MXene spectra is likely attributed to the vibration resulting from the displacement of the Ti-O bond [57]. Following the reaction with APTES, a distinct peak at 910 cm⁻¹ and a band at 950 cm⁻¹ emerged, indicating the presence of Si–O stretching vibration [58, 59]. In addition, N–H bending is observed at 1640 cm⁻¹.

3.2. Characterizations of MX/PCL nanocomposites

Figure 3 presents the structural, crystalline, and thermal characteristics of the MX/PCL nanocomposites. The FTIR spectra of the composites are shown in figure 3(A). The stretching vibration of the—(CH₂)₄—skeletal group in PCL appeared at PCL around 2860 and 2940 cm⁻¹, and the stretching vibration of C=O group at 1725 cm⁻¹ [44]. According to the FTIR data, the MX/PCL composites were successfully prepared [51]. There is a shift in intensity of peaks appeared at 1725 cm⁻¹ (C=O stretching) with composites containing higher f-MXene values, which can be attributed to stronger interactions between PCL and f-MXene due to hydrogen bonding or dipole interactions. Increased intensity in peaks at \sim 2860 and 2940 cm $^{-1}$ (-CH₂ stretching vibrations) indicates that the polymer matrix structure is affected by the presence of f-MXene, likely due to changes in crystallinity or molecular packing. The observed intensity changes align with increased filler-matrix interactions [60]. The N-H stretching vibrations of the principal amines $(-NH_2)$ present in APTES, which is found in f-MXene and MX/PCL composites, give rise to a wide peak at approximately 3300 cm⁻¹ as shown in figure 3(A) (inset image) [61].

3.3. Characterizations of 3D printed scaffolds

The printing temperature was set higher than the melting temperature of PCL obtain the desired viscosity and readiness to flow upon adjustment of pressure and other printing parameters [62, 63] to obtain fine fibers. 3D MEW was performed for the pristine and MX/PCL nanocomposites.

The digital (figure 4(A)) and SEM (figure 4(B)) images showed the interconnected porous architecture and structural integrity of 3D-printed scaffolds. Filament diameter and inter-layer gap distance of the printed structures were quantified using SEM images and ImageJ software, and results showed the printability of the nanocomposite with structural uniformity. The fiber diameters (figure 4(C)) and gap distances (figure 4(D)) were measured from various layers. Each measurement was presented as the mean value of 15 random sites within the 3D-printed scaffold. The structural stability was evaluated by calculating the standard deviation of the obtained values.

The fiber diameter of the 3D-printed MX/PCL scaffolds (figure 4(C)) shows how crystallization

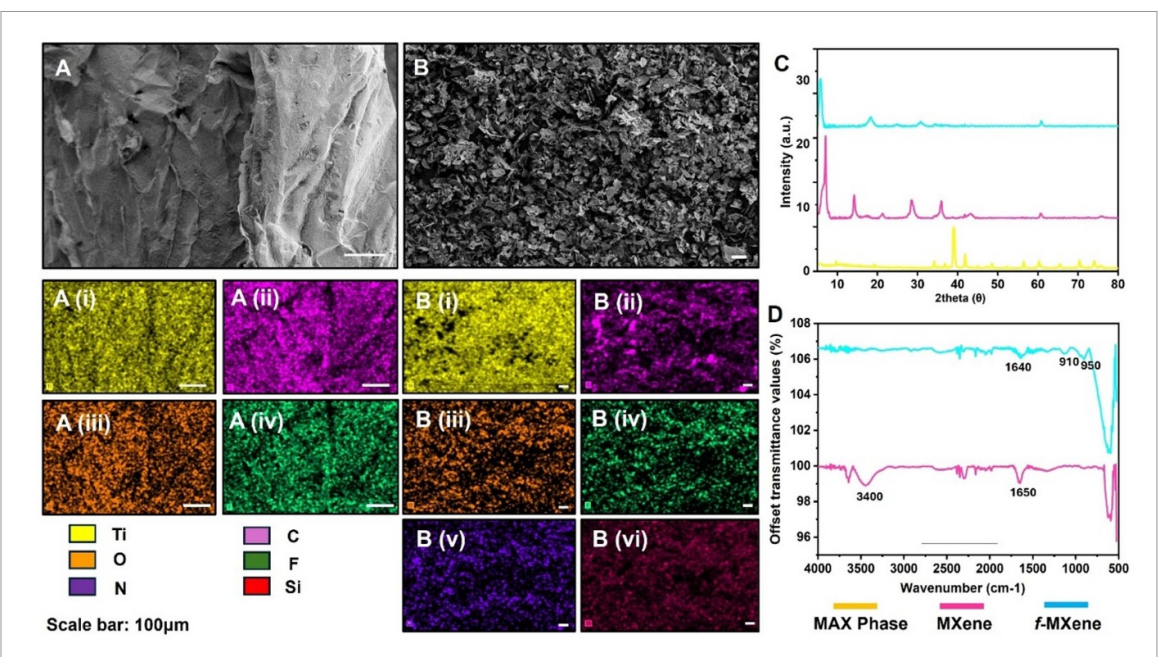


Figure 2. Characterization of MXene and f-MXene. SEM image of MXene shows the (A) 2D nanosheet structure and SEM/EDS analysis (A-i, ii, iii, iii and iv) reveals the elemental composition (Ti, O, C, F). (B) SEM image of f-MXene shows the crumbled 2D nanostructures and SEM/EDS analysis (B-i, ii, iii, iv, v, and vi) reveals the elemental composition and APTES modification (Ti, O, C, N, and Si). Scale bars show 100 μ m (C) XRD patterns indicate preserved crystalline structure of MXene after functionalization. (D) FTIR spectra demonstrates successful functionalization of MXene with APTES with emerged Si–O–Ti and Si–O–Si bonds.

behavior and extrusion dynamics during MEW interact. From the cooling cycle DSC data, adding *f*-MXene to the PCL matrix changed the crystallization temperatures, which affected the solidification followed by deposition. EDS mapping results (figure 5) demonstrated a uniform distribution of *f*-MXene elements in the 3D-printed scaffolds. The data are reported only for 1% MX/PCL composite scaffolds as a demonstration of good distribution at the highest concentration.

The effect of the f-MXene reinforcement on the mechanical properties of the MX/PCL scaffolds was assessed by performing compressive tests. A load case was applied to the pristine and MX/PCL scaffolds using DMA. The compressive modulus in figure 6(B) shows an increase from 1.33 + 0.05 MPa to 6.5 \pm 0.12 MPa with increasing MXene content. This can be attributed to the inherent rigidity of the MXene nanosheets and their uniform dispersion within the polymer matrix, which restricts chain mobility and enhances load transfer. These results demonstrate that incorporating MXene into PCL scaffolds enhances both the stiffness and strength of the scaffolds in a concentration-dependent manner. This can be attributed to the inherent rigidity of the MXene nanosheets and their uniform dispersion within the polymer matrix, which restricts chain mobility and enhances load transfer.

In terms of yield strength (figure 6(B)), a similar increasing trend is observed with increasing MXene content. The yield strength increases from 0.28 \pm 0.08 MPa for pristine PCL to 1.22 \pm 0.09 MPa for the 1% MX/PCL composite. Notably, all MX/PCL

composites exhibit higher yield strength than pristine PCL, with the 0.1% and 0.5MX/PCL composite showing 0.53 \pm 0.03 and 1.12 \pm 0.06 values, respectively. This improvement highlights the reinforcing role of MXene in enhancing the scaffold's capacity to withstand deformation before yielding, which is critical for load-bearing applications.

Furthermore, a reduction in strain capacity is observed, decreasing from approximately 80% for pristine PCL to 50% for 1% MX/PCL. This concentration-dependent reduction in strain is attributed to disruption of interpolymeric interactions, thereby limiting the polymer's elasticity. This trend is consistent with literature reports on 2D–polymer composites [64].

3.3.1. Printing optimization results

As apparent from the fiber size diameter data represented in supporting information, the results indicate the same interplay between the printing parameters and the obtained fiber diameter across all MX/PCL concentration. Detailed examination of the response surface methodology analysis is beyond the scope of this study and are not included here, but the established baseline guided the selection of appropriate printing conditions for subsequent evaluations.

This approach confirmed that although the external parameters remained fixed, intrinsic material properties—most notably viscosity as inferred from DSC—contributed to determining fiber diameter. As MXene content increased, viscosity increased accordingly, leading to measurable, though controlled, increases in fiber diameter.

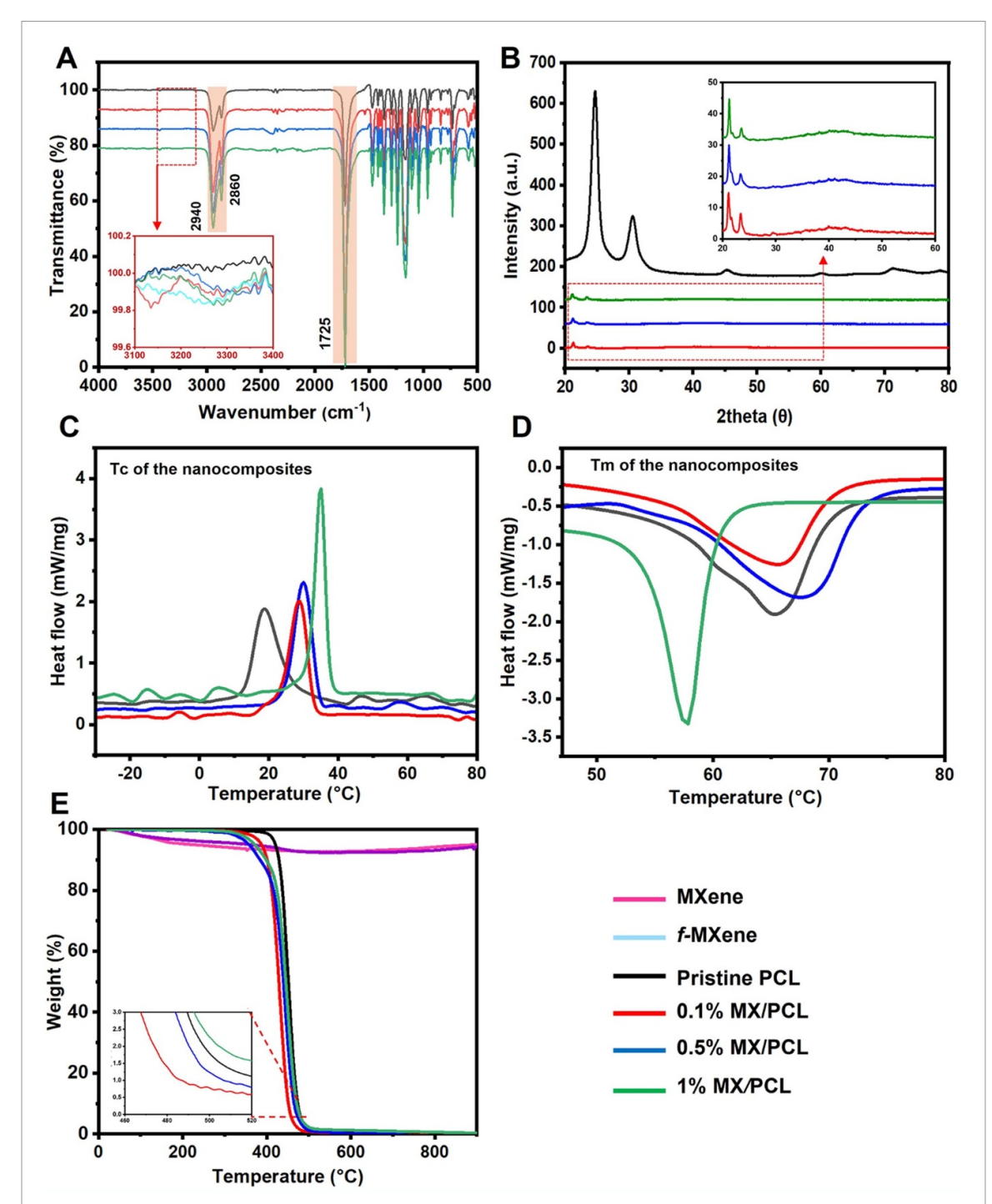


Figure 3. Structural, chemical, and thermal characteristics of nanocomposites prepared in various concentrations of f-MXene. (A) FTIR spectra (inset image for the 3100-3400 cm $^{-1}$ region demonstrating the presence of APTES in nanocomposites, with key peaks labeled and color-coded for different MX/PCL nanocomposite concentrations), (B) XRD spectra (inset image for a zoomed-in view of nanocomposites, highlighting diffraction peaks corresponding to f-MXene and other phases), (C) DSC curves for the cooling cycle (with Tm, and Tc), (D) DSC curves for the heating cycle, and (E) TGA analysis (inset image of the decomposition region, with onset decomposition temperatures).

The results we obtained are compatible with a literature report for modeling MEW of PCL with the same 4 continuous factors in determining the fiber diameter response [65].

Although we aimed to achieve fiber diameters of approximately 100 μ m using a different set of printing parameters, our optimized RSM model suggested that different parameter combinations are required to reproduce these fiber sizes consistently.

This discrepancy is partly attributed to the trade-off between achieving finest fiber diameters and maintaining overall print quality and shape fidelity, especially considering the higher viscosity of composite formulations.

The experiment design analysis was particularly valuable for revealing how MXene/PCL composites respond to variations in printing parameters compared to neat PCL, highlighting the influence of

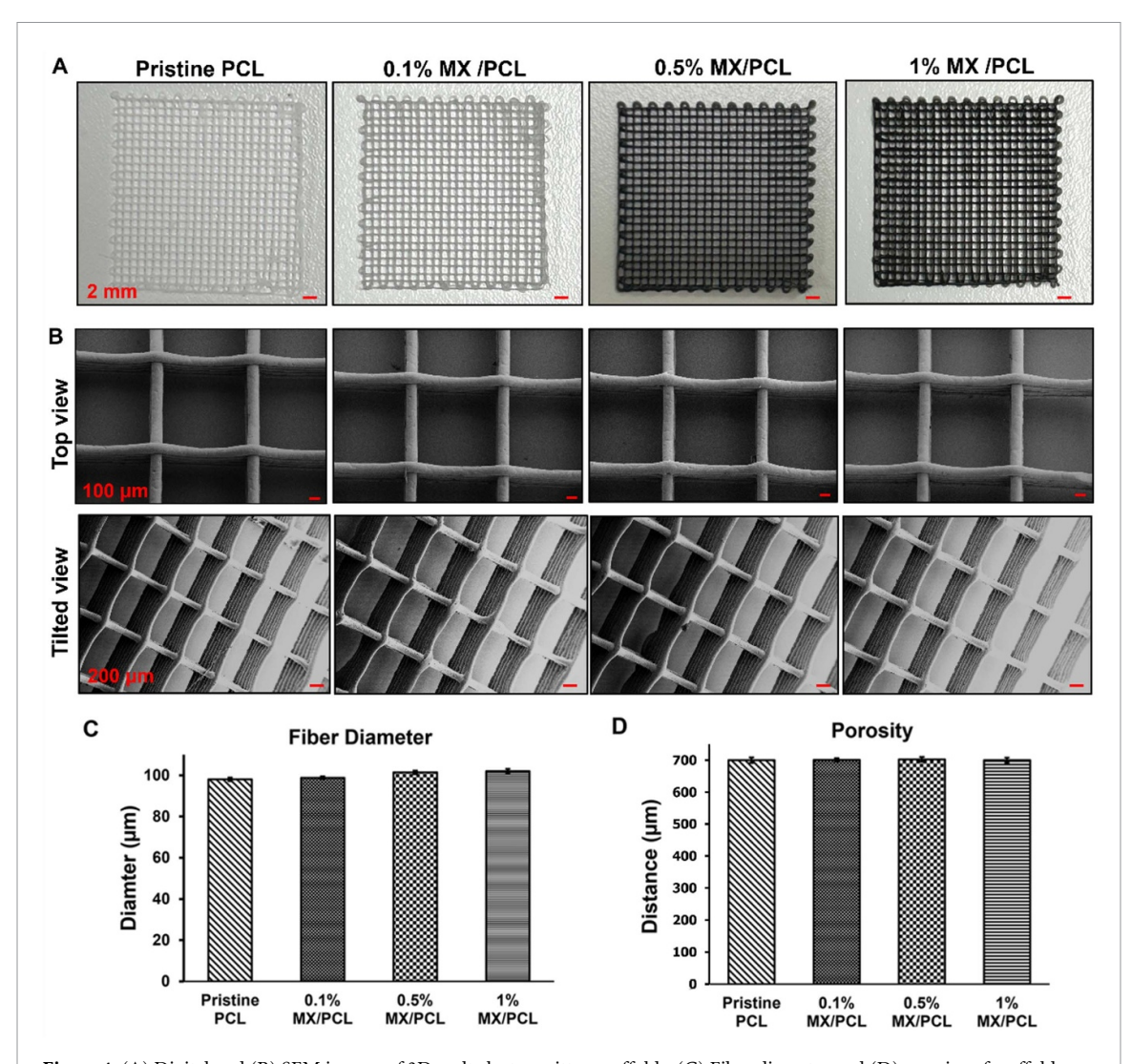
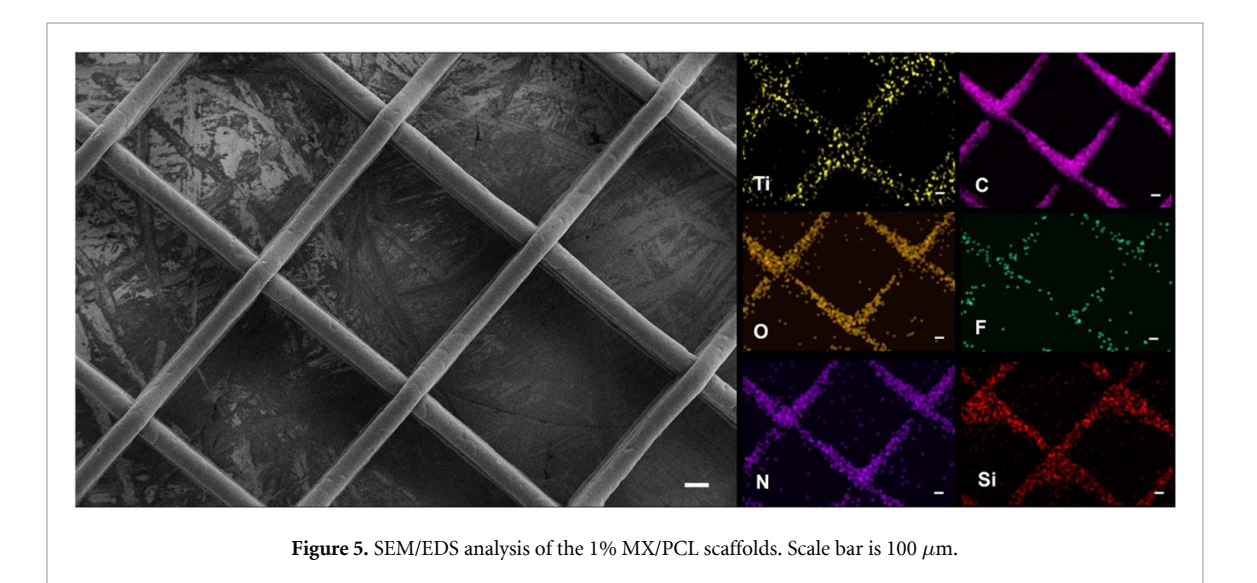


Figure 4. (A) Digital and (B) SEM images of 3D melt electrowritten scaffolds. (C) Fiber diameter and (D) gap size of scaffolds measured using imagej.



different viscosities on fiber formation. Although the parameter space originally included high printing speeds to evaluate extreme elongation effects on fiber diameter, the final printing speed was set to 110 mm min⁻¹—a compromise that minimized defects such as edge irregularities and ensured consistent fiber formation across all concentrations, without coiling effect. To maintain scaffold quality,

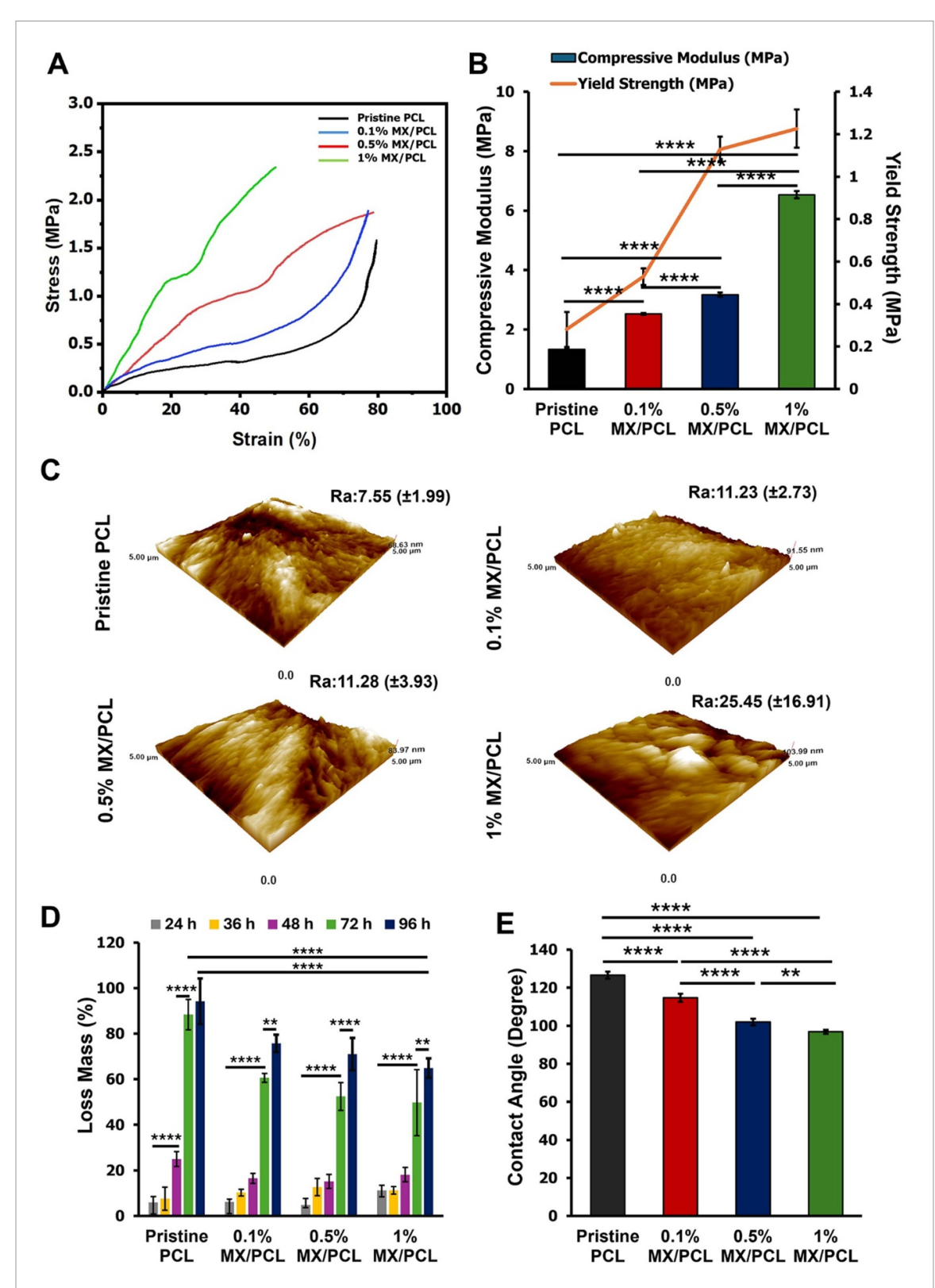


Figure 6. Structural characterization of the nanocomposite scaffolds. (A) Stress–strain curve obtained from compression test, and (B) compressive modulus and yield strength of pristine PCL and nanocomposite scaffolds (n=5). (C) AFM results indicating roughness values as mean \pm SD (D) accelerated degradation and (E)Contact angle measurement. Significance difference between the groups was analyzed using one-way ANOVA for compressive modulus and contact angle measurements while two-way ANOVA in combination with Bonferroni tests was used to analyze the significant degradation rate. p < 0.05 (*), p < 0.005 (**), and p < 0.0001 (****) are used to show the significance levels.

the lowest feasible printing speed was selected, while feeding pressure and voltage were adjusted according to the obtained results to compensate for fiber diameter variations and achieve the target printing performance.

After conducting the experiments, the diameter of the printed fibers was measured using imaging techniques.

This results essentially provides a framework for selecting a combination of collector speed, tip-to-collector distance, and pressure to achieve a desired fiber diameter during melt electrowritting.

The PCL used in this study was relatively low to medium MW, contributing to a manageable melt viscosity that is well-suited for thermal processing and electrohydrodynamic printing. Among the compositions, pristine PCL served as the baseline. The addition of MXene, even at low concentrations, led to changes in thermal behavior, with slight variations observed in melting enthalpy, as apparent in DSC results, and crystallinity. These differences reflect the impact of MXene on polymer chain organization and mobility, which in turn influences the viscosity of the molten material.

While the fiber diameter remained within an acceptable and functional range across all compositions, slight differences were observed. These can be attributed to the gradual increase in viscosity resulting from filler—matrix interactions as MXene concentration increased. The 1% MXene/PCL composite, in particular, exhibited the highest melting enthalpy and implied the most pronounced increase in viscosity due to stronger filler-induced structuring. This higher viscosity led to a more limited elongation of the molten jet, resulting in slightly thicker fibers compared to the lower concentration groups.

Specifically, the model indicates that the smallest fiber diameter is achieved with a combination of high collector speed, low feeding pressure, and a shorter tip-to-collector distance. This is attributed to increased pulling force from the higher speed (which thins the fiber), higher flow rate at increased pressure (which thickens the fiber), and the non-linear interplay between tangential electrical stress and tensile forces along the tip-to-collector distance. Overall, pressure, collector speed, and tip-to-collector distance emerged as the key factors influencing fiber diameter, confirming the relevance of these parameters for MXene/PCL printing.

Topographical characterization conducted via AFM for 3D MEW MX/PCL scaffolds are shown in figure 6(C). The values are reported as mean \pm SD. Roughness of 0.1% and 0.5% MX/PCL scaffolds are higher compared to pristine PCL. The highest roughness is seen in the 1% MX/PCL scaffolds.

According to XRD results, the interlayer distances, calculated using the Bragg equation, are 9.1 Å for MAX phase, 12.52 Å for MXene, and 15.22 Å for

APTES-MXene (figure 2(C)). Crystallographic studies and changes in defects are out of the scope of this study since we were interested in chemistry and the interaction between f-MXene and pristine PCL exhibits a distinct peak at around $2\theta = 24.5^{\circ}$, ° and 30.5° corresponding to its semi-crystalline orthorhombic structure. The addition of 0.1% MX/PCL results in a slight broadening and reduced intensity of this peak, suggesting minimal disruption to the crystalline structure of PCL (figure 3(B)-inset). A further reduction in peak intensity is observed with higher f-MXene concentrations. This disruption may imply good dispersion of f-MXene within the PCL matrix.

In the 3D MEW process, the processing temperature of materials is crucial. Numerous research has already addressed the relationship between process temperature, melted viscosity and chemical stability of the polymers [66–68]. The chemical stability of the polymer might be affected upon increased processing temperature of thermoplastics which might lead to thermal decomposition [69]. The DSC data were taken into consideration while designing the 3D MEW printing parameters for the nanocomposites. Incorporating MXene into PCL affected crystallization behaviors, with the impact differing according to the MXene concentration (figure 3(C)).

Pristine PCL exhibits a melting point of 65.3 °C, whereas 0.1% and 0.5% MX/PCL nanocomposites demonstrate marginal increases to 65.6 °C and 67.6 °C, respectively, indicating negligible disruption at lower MXene concentrations. At 1% MX/PCL, the melting point considerably decreases to 57.8 °C. This reduction in melting point of 1% MX/PCL can be attributed to the thermal conductivity of the MXene with more pronounced effect at the highest concentration among other groups [64]. Pristine PCL crystallizes at 19 °C, whereas 0.1% and 0.5% MX/PCL demonstrate elevated crystallization temperatures of 28.42 °C and 30 °C, respectively, indicating that MXene functions as a nucleating agent, accelerating the crystallization process. The 1% MX/PCL sample has the greatest crystallization temperature at 35 °C, suggesting accelerated crystallization, presumably because of the many nucleation sites offered by MXene. The large surface area of MXene enhances interface interactions with PCL, thereby impacting the crystalline structure of PCL. Accelerated crystallization results in a heightened exothermic peak, leading to expedited solidification. This higher temperature ensures that the struts solidify more quickly, leading to reduced shape distortion.

The thermal stability of f-MXene, PCL, and MX/PCL composites were assessed using TGA (figure 2(d)). MXene displayed minimal weight loss, which could be attributed to the removal of adsorbed water and the surface functionalities, indicating a high degree of thermal stability.

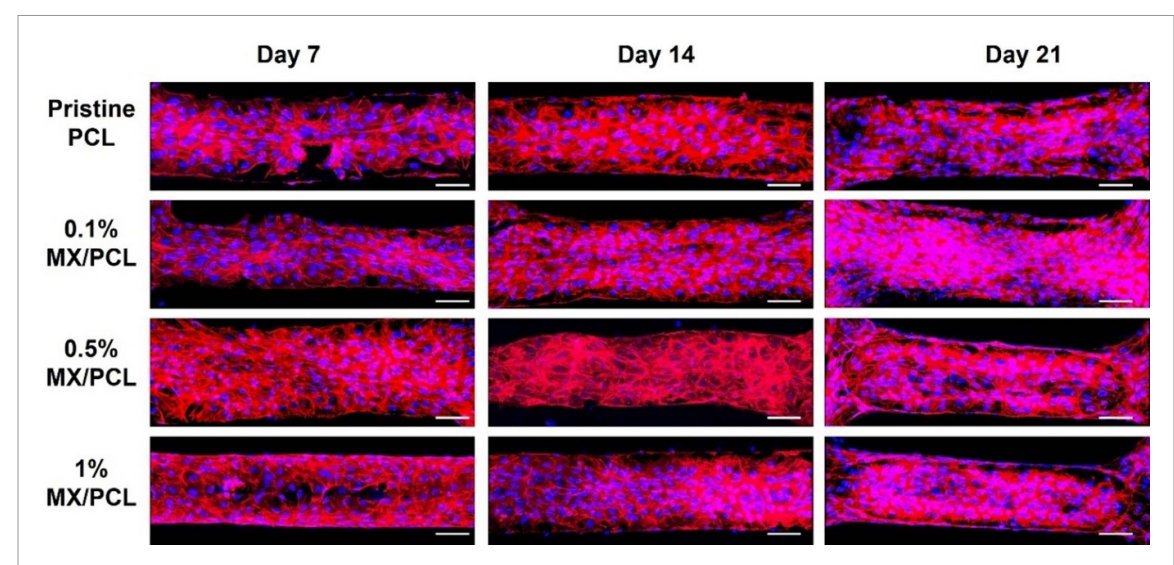


Figure 7. Confocal microscopy images of MC3T3 cells seeded on 3D melt electrowritten MX/PCL nanocomposite scaffolds. Phalloidin/DAPI staining was performed to stain cytoskeleton (red) and nuclei (blue) of the adhered cells on days 7, 14, and 21. Scale bars show $50 \mu m$.

f-MXene decomposed at the same temperature range, indicating that the decomposition behavior of the MXene scaffold remained unaffected by the silane functionalization process. The weight loss observed after 400 °C was attributed to the covalent bonding of APTES to the MXene surface, which aligns with literature [49]. The MX/PCL composites demonstrated superior thermal stability, with the decomposition temperatures of both pristine PCL and MX/PCL composites being significantly higher than the melt electrowritting processing temperature (70 °C-75 °C). This ensures that no decomposition occurs during MEW, and the remaining weight after polymer decomposition is attributable to the f-MXene content [70]. PCL is a semi-crystalline, hydrophobic aliphatic polyester that is a commonly used scaffold material for bone tissue engineering studies. As a long-term stable polymer, PCL undergoes hydrolytic degradation and requires 2-4 years for complete degradation depending on MW [71]. In vitro degradation of PCL scaffolds after 6 months often shows good biocompatibility, minimal mass loss and no adverse host tissue reactions. We performed an accelerated degradation assay by immersing the pristine and MX/PCL MEW scaffolds in a high concentration NaOH solution for 96 h [72, 73]. In the first 24 h, we did not observe a significant degradation rate for the scaffolds as demonstrated in figure 6(D). In later time points, we found that the incorporation of f-MXene significantly delayed the degradation rate of PCL scaffolds. A significant mass loss of about 30% was observed after 48 h treatment of pristine PCL compared to that at 24 h while a noticeable weight loss (60%) from MX/PCL scaffolds was observed later time point which was at 72 h regardless of the f-MXene concentration.

However, the weight loss rate was lower, and the remaining mass of MX/PCL scaffolds was higher than the weight remaining from the pristine PCL which was 10% on 72 h. After 96 h treatment, almost 100% pristine PCL scaffold was degraded while MX/PCL scaffolds retained almost 25% weight. These results showed that f-MXene incorporation lowers the degradation rate of ultra-thin fibers of PCL scaffolds. We further analyzed the WCA of the composite scaffolds to gain a better understanding of the impact of composition on scaffold wettability (figure 6(E)). The composites had a decreasing trend in their WCA as the concentration of MXene increased. The primary component responsible for lowering the WCA in MXene was the presence of oxygen functionalities, which act as a hydrogen bonding acceptor. In other words, the affinity of water to the scaffold surface increased due to hydrogen bonding, and thus, the scaffold hydrophilicity increased significantly as the concentration of f-MXene increased in the 3D printed composite scaffold.

3.4. Cytocompatibility and osteogenic assessments

The series of characterization results demonstrated that *f*-MXene filler induced significant differences in the physical and biochemical properties of the MEW PCL scaffolds. This change is critical for cytocompatibility since the cells come into contact with the scaffold surface for adhesion which is important to regulate cellular behaviors including proliferation and differentiation. We investigated the cytocompatibility and osteoinductive properties of the MX/PCL nanocomposite scaffolds by using MC3T3-E1 preosteoblast cells. Figure 7 shows the confocal microscopy images of cells representing the cytoskeleton and nuclei of the adhered cells onthe

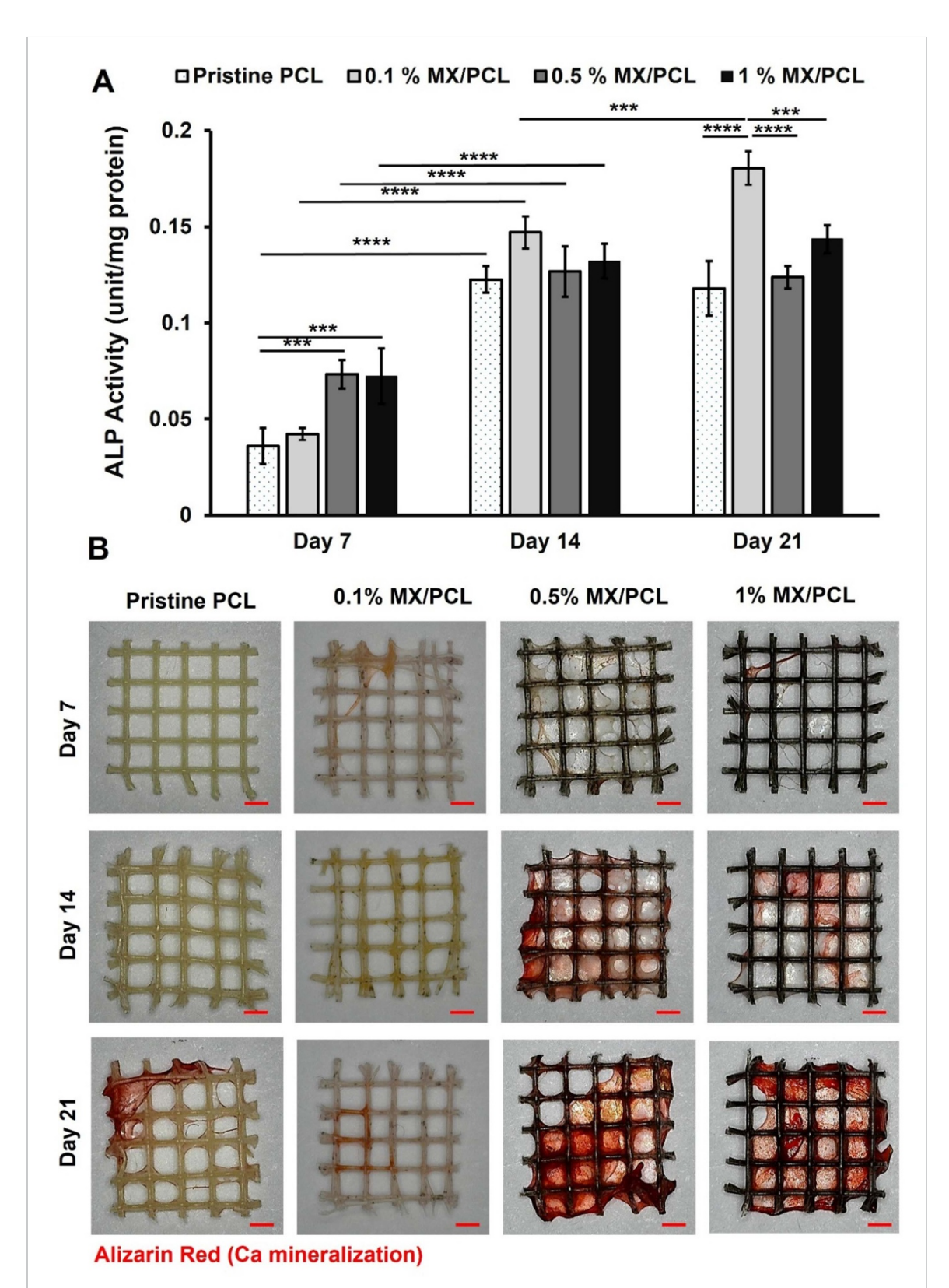


Figure 8. Osteoinductive properties of 3D melt electrowritten scaffolds. (A) ALP activity assessed after incubation of MC3T3 cell on pristine and MXene/PCL nanocomposite scaffolds for 7, 14, and 21 d. Four replicates were used for each condition and the data was normalized to the total protein concentration. Significance difference between the groups was analyzed using two-way ANOVA in combination with Bonferroni tests. p < 0.001 (***), and p < 0.0001 (****) are used to show the significance levels. (B) Alizarin red staining was conducted to show mineralization on days 7, 14 and 21. Scale bars show 1 mm.

MX/PCL scaffolds over a 21 d incubation period. Regardless of the MXene concentration, the strong adherence of the preosteoblast to MEW scaffolds was observed on day 7. On days 14 and 21, the cells spread and formed fully covered confluent layers on the scaffold surface. These results indicated that MX/PCL scaffolds are favorable for cell adhesion and proliferation.

A change in cellular behavior is expected due to the variation of surface properties. ALP activity assay and alizarin red staining were conducted to evaluate the osteogenic differentiation of preosteoblasts in response to the mechanical and physicochemical properties of the MEW PCL scaffolds (figure 8). The significant increase in the ALP activity of the preosteoblasts adhered to 0.5% and 1% (w/w) MX/PCL scaffolds compared to the pristine scaffolds on day 7 revealed enhanced osteogenic differentiation (figure 8(A)). A remarkable increase in ALP activity on day 14 was observed for all conditions, but there were no significant changes between the groups. On day 21, a significant increase in ALP activity was observed only for preosteoblasts that were seeded on 0.1% (w/w) MX/PCL scaffolds. ALP is the marker for the early stages of osteogenic differentiation and their activity decreases as the ECM matures, and mineralization starts [74, 75]. These results revealed that the early osteogenic differentiation was initiated for the preosteoblasts seeded on 0.5% and 1% (w/w) MX/PCL scaffolds on day 7.

The non-significant change in the later time points is expected due to the initiation of mineral deposition. At the later time point on day 21, the increase in ALP activity for the cells seeded on 0.1% (w/w) MX/PCL scaffolds compared to the pristine PCL scaffolds also indicated the effect of f-MXene incorporation on osteoinductivity of the PCL scaffolds. Further evaluation using alizarin red staining the mineralization of 0.1% (w/w) MX/PCL scaffolds started, as expected. Overall, the ALP activity and mineralization results revealed the enhanced differentiation of MC3T3-E1 preosteoblast cells on MX/PCL scaffolds. The differentiation of cells and mineralization depended on variations in the scaffold properties affected proportionally by the concentration of the f-MXene. The mechanism could be attributed to the hydrophilic properties of MX/PCL scaffold variations which could increase surface-to-cell interaction and thus, cell adhesion and proliferation of preosteoblasts. Additionally, the mechanotransduction and mechanosensing of the cells are also anticipated to have a significant role in osteogenic enhancement, as they vary depending on the concentration of the f-MXene incorporated in PCL matrix. These results are consistent with literature reports

on osteogenic differentiation mechanisms specifically for the graphene-loaded PCL scaffolds [76–78].

4. Conclusion

In the study, MXene was synthesized and functionalized with APTES. The f-MXene showed enhanced compatibility with PCL, improving dispersion within the PCL matrix. The extrudability of the filaments under high voltage for the resulting composites with 0.1%, 0.5%, and 1% (w/w) MX/PCL ratios were demonstrated using melt electrowriting in high shape fidelity, and accuracy. TGA and DSC analyses of MX/PCL nanocomposites with 0.1, 0.5, and 1% (w/w) loadings showed the thermal stability of f-MXene during the MEW process and determined the optimal MEW operating conditions respectively. The printability of all compositions using MEWin 0°-90° mesh scaffolds was demonstrated using morphological characterization via SEM and EDS mapping, which indicated structural integrity for all printed structures. Further characterization confirmed the concentration-dependent enhancement in hydrophilicity and compressive modulus and yield strength of scaffolds upon integration of MXene. The incorporation of MXene into PCL was indicated to increase the roughness with the highest increase in the 1% MX/PCL scaffolds. Accelerated degradation tests demonstrated that increasing filler concentration in the reinforced scaffolds progressively delayed degradation compared to the control. The MX/PCL scaffolds showed the biocompatibility demonstrated by the efficient adherence of preosteoblast cells on MX/PCL scaffolds. The MX concentration within the PCL filaments enhanced differentiation of preosteoblast cells and mineralization. The findings of the study indicate that 3D printed nanocomposite scaffolds, made of thermoplastic PCL reinforced with low loading amounts of f-MXene, have significant potential as suitable scaffolds for bone tissue engineering applications as mechanically robust properties with controlled degradation rates and favorable bioactivity.

Data availability statement

All data that support the findings of this study are included within the article (and any supplementary files).

Acknowledgment

This work was financially supported by Sabanci University Nanotechnology Research and Application Center (SUNUM), and FLAG-ERA Grant [GRAPH-OCD], by the Scientific and Technological Research Council of Turkey (TUBITAK) [223N171].

ORCID iDs

References

- [1] Seiti M, Ginestra P, Ferraro R M, Ceretti E and Ferraris E 2020 Nebulized jet-based printing of bio-electrical scaffolds for neural tissue engineering: a feasibility study *Biofabrication* 12 025024
- [2] Zhao Y, Song S, Ren X, Zhang J, Lin Q and Zhao Y 2022 Supramolecular adhesive hydrogels for tissue engineering applications Chem. Rev. 122 5604–40
- [3] Yu Z et al 2023 3D conductive scaffolds of MXene@PCL with high conductivity and small line width fabricated by electric-field-driven jet 3D printing and electrostatic self-assembly Mater. Today Commun. 35 105704
- [4] Xie F, Cao H, Ma L, Hua X and Li C 2021 Biofabrication of controllable tubular calcium alginate hydrogel for tissue engineering J. Mater. Res. 36 1487–95
- [5] Makris E A, Gomoll A H, Malizos K N, Hu J C and Athanasiou K A 2015 Repair and tissue engineering techniques for articular cartilage *Nat. Rev. Rheumatol.* 11 21–34
- [6] Karimi M, Asefnejad A, Aflaki D, Surendar A, Baharifar H, Saber-Samandari S, Khandan A, Khan A and Toghraie D 2021 Fabrication of shapeless scaffolds reinforced with baghdadite-magnetite nanoparticles using a 3D printer and freeze-drying technique J. Mater. Res. Technol. 14 3070–9
- [7] Namvari M, Inan T and Altan A 2023 MXene-cellulose nanofiber composites: toward green, multi-functional, flexible, and highly efficient electromagnetic interference shielding materials *Graphene 2D Mater.* 8 5–26
- [8] Sayyar S, Murray E, Thompson B C, Chung J, Officer D L, Gambhir S, Spinks G M and Wallace G G 2015 Processable conducting graphene/chitosan hydrogels for tissue engineering J. Mater. Chem. B 3 481–90
- [9] Cipitria A, Skelton A, Dargaville T, Dalton P and Hutmacher D 2011 Design, fabrication and characterization of PCL electrospun scaffolds—a review J. Mater. Chem. 21 9419–53
- [10] Sayyar S, Officer D L and Wallace G G 2017 Fabrication of 3D structures from graphene-based biocomposites J. Mater. Chem. B 5 3462–82
- [11] Hoque M E, Chuan Y L and Pashby I 2012 Extrusion based rapid prototyping technique: an advanced platform for tissue engineering scaffold fabrication *Biopolymers* 97 83–93
- [12] Cardwell R D, Dahlgren L A and Goldstein A S 2014 Electrospun fibre diameter, not alignment, affects mesenchymal stem cell differentiation into the tendon/ligament lineage J. Tissue Eng. Regen. Med. 8 937–45
- [13] Christopherson G T, Song H and Mao H-Q 2009 The influence of fiber diameter of electrospun substrates on neural stem cell differentiation and proliferation *Biomaterials* 30 556–64
- [14] Afghah F, Dikyol C, Altunbek M and Koc B 2019 Biomimicry in bio-manufacturing: developments in melt electrospinning writing technology towards hybrid biomanufacturing Appl. Sci. 9 3540
- [15] Afghah F, Altunbek M, Zahrabi M and Koc B 2025 Microstructural effects of melt electrowritten-reinforced hydrogel scaffolds for engineering thick skin substitutes ACS Appl. Bio Mater. 8 2875–87
- [16] Kaur G, Adhikari R, Cass P, Bown M and Gunatillake P 2015 Electrically conductive polymers and composites for biomedical applications RSC Adv. 5 37553–67

- [17] Thompson B C, Murray E and Wallace G G 2015 Graphite oxide to graphene. Biomaterials to bionics Adv. Mater. 27 7563–82
- [18] Pinto A M, Goncalves I C and Magalhaes F D 2013 Graphene-based materials biocompatibility: a review Colloids Surf. B 111 188–202
- [19] Sun H, Mei L, Song C, Cui X and Wang P 2006 The in vivo degradation, absorption and excretion of PCL-based implant Biomaterials 27 1735—40
- [20] Sánchez-González S, Diban N and Urtiaga A 2018 Hydrolytic degradation and mechanical stability of poly (ε-Caprolactone)/reduced graphene oxide membranes as scaffolds for *in vitro* neural tissue regeneration *Membranes* 8 12
- [21] Abdal-hay A, Sheikh F A, Gómez-Cerezo N, Alneairi A, Luqman M, Pant H R and Ivanovski S 2022 A review of protein adsorption and bioactivity characteristics of poly ε-caprolactone scaffolds in regenerative medicine Eur. Polym. J. 162 110892
- [22] Wang W *et al* 2019 Engineered 3D printed poly (ε-caprolactone)/graphene scaffolds for bone tissue engineering *Mater. Sci. Eng. C* 100 759–70
- [23] Sahafnejad-Mohammadi I, Rahmati S, Najmoddin N and Bodaghi M 2023 Biomimetic polycaprolactone-graphene oxide composites for 3D printing bone scaffolds *Macromol. Mater. Eng.* 308 2200558
- [24] Khoei J K, Bafqi M S S, Saeidiharzand S, Mohammadilooey M, Hezarkhani M, Okan B S, Koşar A and Sadaghiani A K 2023 Upcycled graphene integrated fiber-based photothermal hybrid nanocomposites for solar-driven interfacial water evaporation *Desalination* 562 116707
- [25] Meng D, Hou Y, Kurniawan D, Weng R-J, Chiang W-H and Wang W 2024 3D-Printed graphene and graphene quantum dot-reinforced polycaprolactone scaffolds for bone-tissue engineering ACS Appl. Nano Mater. 7 1245–56
- [26] Altan A and Namvari M 2023 Multifunctional, flexible, and mechanically robust polyimide-MXene nanocomposites: a review 2D Mater. 10 042001
- [27] Zhong Y, Huang S, Feng Z, Fu Y and Mo A 2022 Recent advances and trends in the applications of MXene nanomaterials for tissue engineering and regeneration J. Biomed. Mater. Res. A 110 1840–59
- [28] Downes M, Shuck C E, McBride B, Busa J and Gogotsi Y 2024 Comprehensive synthesis of Ti₃C₂T_x from MAX phase to MXene Nat. Protoc. 19 1–28
- [29] Naguib M, Kurtoglu M, Presser V, Lu J, Niu J, Heon M, Hultman L, Gogotsi Y and Barsoum M W 2011 Two-dimensional nanocrystals produced by exfoliation of Ti₃A₁C₂, MXenes Adv. Mater. 23 4248–53
- [30] Zhang Z et al 2022 Ti₃C₂T_xMXene composite 3D hydrogel potentiates mTOR signaling to promote the generation of functional hair cells in cochlea organoids Adv. Sci. 9 2203557
- [31] Kabir L, Qi J, Wijaya K, Sagadevan S, Yoon C-M, Ullah K and Oh W-C 2024 Recent advances and latest technologies in energy storage applications based on 2D MXene J. Energy Storage 80 110335
- [32] Namvari M and Chakrabarti B K 2024 Electrophoretic deposition of MXenes and their composites: toward a scalable approach Adv. Colloid Interface Sci. 331 103208
- [33] Zhou H, Han S J, Lee H-D, Zhang D, Anayee M, Jo S H, Gogotsi Y and Lee T-W 2022 Overcoming the limitations of MXene electrodes for solution-processed optoelectronic devices Adv. Mater. 34 2206377
- [34] Jin C and Bai Z 2022 MXene-based textile sensors for wearable applications ACS Sens. 7 929–50
- [35] Park H, Kim S, Kim S, Kim M, Kang Y, Amirthalingam S, Lee S, Hwang N S, Yang K and Kim H D 2023 Bioactive inorganic compound MXene and its application in tissue engineering and regenerative medicine J. Ind. Eng. Chem. 117 38–53

- [36] Wang J, Shen M, Liu Z and Wang W 2022 MXene materials for advanced thermal management and thermal energy utilization Nano Energy 97 107177
- [37] Jena R K, Das H T, Patra B N and Das N 2022 MXene-based nanomaterials as adsorbents for wastewater treatment: a review on recent trends Front. Mater. Sci. 16 220592
- [38] Maleki A *et al* 2022 Biomedical applications of MXene-integrated composites: regenerative medicine, infection therapy, cancer treatment, and biosensing *Adv. Funct. Mater.* 32 2203430
- [39] Diedkova K et al 2023 Polycaprolactone–MXene nanofibrous scaffolds for tissue engineering ACS Appl. Mater. Interfaces 15 14033–47
- [40] Bai Y et al 2016 Characterization, corrosion behavior, cellular response and in vivo bone tissue compatibility of titanium—niobium alloy with low young's modulus Mater. Sci. Eng. C 59 565–76
- [41] Cui D, Kong N, Ding L, Guo Y, Yang W and Yan F 2021 Ultrathin 2D titanium carbide MXene (Ti(3) C(2) T(x)) nanoflakes activate WNT/HIF-1alpha-mediated metabolism reprogramming for periodontal regeneration Adv. Healthcare Mater. 10 e2101215
- [42] Guo R, Xiao M, Zhao W, Zhou S, Hu Y, Liao M, Wang S, Yang X, Chai R and Tang M 2022 2D Ti₃C₂T_xMXene couples electrical stimulation to promote proliferation and neural differentiation of neural stem cells *Acta Biomater*. 139 105–17
- [43] Li T, Ma J, Wang W and Lei B 2023 Bioactive MXene promoting angiogenesis and skeletal muscle regeneration through regulating M2 polarization and oxidation stress Adv. Healthcare Mater. 12 2201862
- [44] Xu Z, Zhang Y, Dai H, Wang Y, Ma Y, Tan S and Han B 2022 3D printed MXene (Ti₂A₁N)/polycaprolactone composite scaffolds for *in situ* maxillofacial bone defect repair *J. Ind.* Eng. Chem. 114 536–48
- [45] Youness R A and Taha M A 2024 Role of Ti₃A₁C₂ MAX phase in regulating biodegradation and improving electrical properties of calcium silicate ceramic for bone repair applications Sci. Rep. 14 25811
- [46] Wang H, Hsu Y-C, Wang C, Xiao X, Yuan Z, Zhu Y and Yang D 2024 Conductive and enhanced mechanical strength of Mo₂Ti₂C₃ MXene-based hydrogel promotes neurogenesis and bone regeneration in bone defect repair ACS Appl. Mater. Interfaces 16 17208–18
- [47] Nie R, Sun Y, Lv H, Lu M, Huangfu H, Li Y, Zhang Y, Wang D, Wang L and Zhou Y 2022 3D printing of MXene composite hydrogel scaffolds for photothermal antibacterial activity and bone regeneration in infected bone defect models *Nanoscale* 14 8112–29
- [48] Nan L-P et al 2022 Ti₃C₂T_x MXene-coated electrospun PCL conduits for enhancing neurite regeneration and angiogenesis Front. Bioeng. Biotechnol. 10 850650
- [49] Li J, Hashemi P, Liu T, Dang K M, Brunk M G K, Mu X, Nia A S, Sacher W D, Feng X and Poon J K S 2024 3D printed titanium carbide MXene-coated polycaprolactone scaffolds for guided neuronal growth and photothermal stimulation Commun. Mater. 5 62
- [50] Zhang G, Wang T, Xu Z, Liu M, Shen C and Meng Q 2020 Synthesis of amino-functionalized Ti₃ C₂T_x MXene by alkalization-grafting modification for efficient lead adsorption Chem. Commun. 56 11283–6
- [51] Riazi H, Anayee M, Hantanasirisakul K, Shamsabadi A A, Anasori B, Gogotsi Y and Soroush M 2020 Surface modification of a MXene by an aminosilane coupling agent Adv. Mater. Interfaces 7 1902008
- [52] Seo O B, Saha S, Kim N H and Lee J H 2021 Preparation of functionalized MXene-stitched-graphene oxide/poly (ethylene-co-acrylic acid) nanocomposite with enhanced hydrogen gas barrier properties J. Membr. Sci. 640 119839
- [53] Ghidiu M, Lukatskaya M R, Zhao M-Q, Gogotsi Y and Barsoum M W 2014 Conductive two-dimensional titanium carbide 'clay' with high volumetric capacitance *Nature* 516 78–81

- [54] Daskalakis E, Hassan M H, Omar A M, Acar A A, Fallah A, Cooper G, Weightman A, Blunn G, Koc B and Bartolo P 2023 Accelerated degradation of poly-ε-caprolactone composite scaffolds for large bone defects *Polymers* 15 670
- [55] Wang C-Y, Kuo Z-K, Hsieh M-K, Ke L-Y, Chen C-C, Cheng C-M and Lai P-L 2019 Cell migration of preosteoblast cells on a clinical gelatin sponge for 3D bone tissue engineering *Biomed. Mater.* 15 015005
- [56] Kumar A N and Pal K 2022 Amine-functionalized stable Nb₂ CT_x MXene toward room temperature ultrasensitive NO 2 gas sensor *Mater. Adv.* 3 5151–62
- [57] Li X et al 2024 Synergistic integration of MXene nanostructures into electrospun fibers for advanced biomedical engineering applications Nanoscale Horiz. 9 1703–24
- [58] Ghaffarian V, Mousavi S M, Bahreini M and Afifi M 2013 Preparation and characterization of biodegradable blend membranes of PBS/CA J. Environ. Polym. 21 1150–7
- [59] Sadeghi B and Pourahmad A 2011 Synthesis of silver/poly (diallyldimethylammonium chloride) hybride nanocomposite Adv. Powder Technol. 22 669–73
- [60] Zhang W-J et al 2022 ROS-and pH-responsive polydopamine functionalized Ti₃C₂T_x MXene-based nanoparticles as drug delivery nanocarriers with high antibacterial activity Nanomaterials 12 4392
- [61] Srivastava S K and Mishra Y K 2018 Nanocarbon reinforced rubber nanocomposites: detailed insights about mechanical, dynamical mechanical properties, payne, and mullin effects Nanomaterials 8 945
- [62] Ko J, Jun S, Lee J K, Lee P C and Jun M B 2015 Effects of molecular weight and temperature on fiber diameter of poly (ε-caprolactone) melt electrospun fiber J. Korean Soc. Manuf. Technol. Eng. 24 160–5
- [63] Yeh C-C, Li Y-T, Chiang P H, Huang C-H, Wang Y and Chang H-I 2009 Characterizing microporous PCL matrices for application of tissue engineering J. Med. Biol. Eng. 29 92–97 (available at: https://www.researchgate.net/profile/ Yiwei-Wang-16/publication/228655673_Characterizing_ Microporous_PCL_Matrices_for_Application_of_Tissue_ Engineering/links/56319c7708ae3de9381d0c3a/ Characterizing-Microporous-PCL-Matrices-for-Application-of-Tissue-Engineering.pdf)
- [64] Chung J H Y, Sayyar S and Wallace G G 2022 Effect of graphene addition on polycaprolactone scaffolds fabricated using melt-electrowriting *Polymers* 14 319
- [65] Dayan C B, Afghah F, Okan B S, Yıldız M, Menceloglu Y, Culha M and Koc B 2018 Modeling 3D melt electrospinning writing by response surface methodology *Mater. Des.* 148 87–95
- [66] Li X, Liu H, Wang J and Li C 2012 Preparation and characterization of poly (ε-caprolactone) nonwoven mats via melt electrospinning *Polymer* 53 248–53
- [67] Sun Y, Matsumoto M, Haruki M, Kihara S-I and Takishima S 2016 Molecular weight dependence of the crystallization of the polycarbonate induced by supercritical CO₂ J. Supercrit. Fluids 113 144–9
- [68] Matta A, Rao R U, Suman K and Rambabu V 2014 Preparation and characterization of biodegradable PLA/PCL polymeric blends Proc. Mater. Sci. 6 1266–70
- [69] Wojtyła S, Klama P and Baran T 2017 Is 3D printing safe? Analysis of the thermal treatment of thermoplastics: ABS, PLA, PET, and nylon J. Occup. Environ. Hyg. 14 D80–D5
- [70] Zhou Z, Panatdasirisuk W, Mathis T S, Anasori B, Lu C, Zhang X, Liao Z, Gogotsi Y and Yang S 2018 Layer-by-layer assembly of MXene and carbon nanotubes on electrospun polymer films for flexible energy storage *Nanoscale* 10 6005–13
- [71] Woodruff M A and Hutmacher D W 2010 The return of a forgotten polymer—Polycaprolactone in the 21st century Prog. Polym. Sci. 35 1217–56
- [72] Mukherjee P, Chung J, Cheng K, Gupta R, Haag H, Williams Z and Wallace G 2021 Invitro and invivo study of

- PCL-hydrogel scaffold to advance bioprinting translation in microtia reconstruction *J. Craniofacial Surg.* **32** 1931–6
- [73] Lam C X F, Hutmacher D W, Schantz J-T, Woodruff M A and Teoh S H 2009 Evaluation of polycaprolactone scaffold degradation for 6 months in vitro and in vivo J. Biomed. Mater. Res. A 90 906–19
- [74] Golub E E and Boesze-Battaglia K 2007 The role of alkaline phosphatase in mineralization *Curr. Opin. Orthop.* 18 444–8
- [75] Grue B H and Veres S P 2022 Effect of increasing mineralization on pre-osteoblast response to native collagen fibril scaffolds for bone tissue repair and regeneration *J. Appl. Biomater. Funct. Mater.* 20 22808000221104000
- [76] Unagolla J M and Jayasuriya A C 2019 Enhanced cell functions on graphene oxide incorporated 3D printed polycaprolactone scaffolds *Mater. Sci. Eng. C* 102 1–11
- [77] Anitasari S, Wu C-Z and Shen Y-K 2023 PCL/Graphene scaffolds for the osteogenesis process *Bioengineering* 10 305
- [78] Ferroni L, Gardin C, Rigoni F, Balliana E, Zanotti F, Scatto M, Riello P and Zavan B 2022 The impact of graphene oxide on polycaprolactone PCL surfaces: antimicrobial activity and osteogenic differentiation of mesenchymal stem cell *Coatings* 12 799

- [79] Abbasi N, Abdal-Hay A, Hamlet S, Graham E and Ivanovski S 2019 Effects of gradient and offset architectures on the mechanical and biological properties of 3-D melt electrowritten (MEW) scaffolds ACS Biomater. Sci. Eng. 5 3448–61
- [80] Jun I, Han H-S, Edwards J R and Jeon H 2018 Electrospun fibrous scaffolds for tissue engineering: viewpoints on architecture and fabrication *Int. J. Mol. Sci.* 19 745
- [81] Liu M, Zhang Y, Sun S, Khan A R, Ji J, Yang M and Zhai G 2019 Recent advances in electrospun for drug delivery purpose J. Drug Target. 27 270–82
- [82] Bružauskaitė I, Bironaitė D, Bagdonas E and Bernotienė E 2016 Scaffolds and cells for tissue regeneration: different scaffold pore sizes—different cell effects Cytotechnology 68 355–69
- [83] Lai Y *et al* 2018 Porous composite scaffold incorporating osteogenic phytomolecule icariin for promoting skeletal regeneration in challenging osteonecrotic bone in rabbits *Biomaterials* 153 1–13
- [84] Hoai T T and Nga N K 2018 Effect of pore architecture on osteoblast adhesion and proliferation on hydroxyapatite/poly (D, L) lactic acid-based bone scaffolds J. Iran. Chem. Soc. 15 1663–71